

## Article

# Enhanced Methane Dry Reforming with Ni/SiO<sub>2</sub> Catalysts Featuring Hierarchical External Nanostructures

Yong Jun Kim , Min-Jae Kim , Dong Hyun Kim, Anush Mnoyan \*  and Kyubock Lee \* 

Graduate School of Energy Science and Technology, Chungnam National University, 99 Daehak-ro, Yuseong-gu, Daejeon 34134, Republic of Korea; yjkimrelentless@gmail.com (Y.J.K.)

\* Correspondence: anush.mnoyan@cnu.ac.kr (A.M.); kyubock.lee@cnu.ac.kr (K.L.);  
Tel.: +82-42-821-8610 (A.M. & K.L.)

**Abstract:** Global energy demand escalates the interest in effective and durable catalytic systems for the dry reforming of methane (DRM), a process that converts CO<sub>2</sub>/CH<sub>4</sub> into H<sub>2</sub>/CO syngas. Porous silica-supported nickel (Ni) catalysts are recognized as a promising candidate due to robust DRM activity associated with the confinement of Ni particles in the mesopores that reduces the catalyst deactivation by carbon byproduct deposits and sintering of active Ni sites. However, the small-sized pore configurations in the mesoporous catalysts hinders the fast mass transfer of reactants and products. A unique combination of the hierarchical nanostructure with macro–mesoporous features of the support is adopted to enhance the catalytic performance via the dual effect of the efficient mass transfer and minimized sintering issue. This study delves into the influence of SiO<sub>2</sub> geometry and pore structure on the catalytic performance of Ni-based catalysts. Three types of porous silica supports were synthesized through various methods: (a) hydrothermal-assisted sol–gel for dendritic mesoporous silica (DMS), (b) spray-pyrolysis-assisted sol–gel for spray evaporation-induced self-assembly (EISA) silica, and (c) oven-assisted sol–gel for oven EISA silica. Among the prepared catalysts the hierarchical external nanostructured Ni/DMS showed the superior CH<sub>4</sub> and CO<sub>2</sub> conversion rates (76.6% and 82.1%), even at high space velocities (GHSV = 360 L·g<sup>-1</sup>·h<sup>-1</sup>). The distinctive macro–mesoporous geometry effectively prevents the sintering of Ni particles and promotes the smooth diffusion of the reactants and products, thus improving catalytic stability over extended reaction periods (24 h). This research highlights the significant impact of macro–mesoporosity revealed in DMS support catalysts on the physicochemical properties of Ni/DMS and their crucial role in enhancing DRM reaction efficiency.

**Keywords:** mesoporous silica; dry reforming of methane; hierarchical nanostructures; pore diffusion resistance



**Citation:** Kim, Y.J.; Kim, M.-J.; Kim, D.H.; Mnoyan, A.; Lee, K. Enhanced Methane Dry Reforming with Ni/SiO<sub>2</sub> Catalysts Featuring Hierarchical External Nanostructures. *Catalysts* **2024**, *14*, 265. <https://doi.org/10.3390/catal14040265>

Academic Editor: Leonarda Liotta

Received: 30 March 2024

Revised: 12 April 2024

Accepted: 13 April 2024

Published: 16 April 2024



**Copyright:** © 2024 by the authors. Licensee MDPI, Basel, Switzerland. This article is an open access article distributed under the terms and conditions of the Creative Commons Attribution (CC BY) license (<https://creativecommons.org/licenses/by/4.0/>).

## 1. Introduction

Dry reforming of methane (DRM) that utilizes two major greenhouse gases as reactants, CH<sub>4</sub> and CO<sub>2</sub>, is one of the promising approaches toward carbon neutrality [1,2]. A mixture of H<sub>2</sub> and CO obtained as products from this reaction can be used as a feedstock for synthesizing various value-added oxygenated chemicals and long-chain hydrocarbons through Fischer–Tropsch reactions [3]. Nickel (Ni)-based catalysts are considered the most promising catalysts for DRM reactions due to their low cost and high catalytic activity similar to noble-metal-based catalysts. However, two main issues of these catalysts are carbon deposits generated from side reactions and sintering of active sites, rapidly deactivating the catalysts [4–7]. One of the practical approaches to address these challenges is confining Ni particles within the channels of mesoporous support materials. The confinement effect mitigates issues related to sintering; the pore structure serves as a physical barrier, effectively preventing Ni sintering [8]. This strategy entails exploiting the robust interaction between embedded Ni particles and the substrate with well-defined mesopores, thereby leading to

a reduction in Ni particle size and enhanced Ni dispersion. Whereas well-defined mesoporous structures allow catalysts with high surface area and the corresponding numbers of active sites, the uniform and small pore size limits the fast mass transfer of reactants and products in the catalysts [9,10].

Several simulation or experimental studies have been carried out to reduce the diffusion limitations of microporous and mesoporous catalysts by introducing macropores and large mesopores in the catalysts. Li et al. introduced macropores into cobalt-based pellet catalysts to overcome the internal diffusion limitations in the Fischer–Tropsch (FT) reaction [11]. The pellet catalyst with macropores showed much higher catalytic activity than the pellet catalyst without macropores, demonstrating the effects of macropores on the performance of FT catalysts. Al-Wang et al. have applied hierarchically structured porous catalysts for the autothermal reforming of methane [12]. By introducing the macropores and optimizing the macroporosity, the overall catalytic efficiency could be enhanced, ranging from 40% to 300%. Halhouli et al. studied the effect of the geometric configuration of four nanostructured catalysts on mass transfer and catalytic activity based on 3D simulations [13]. The four nanostructures are (1) vertical grown cylindrical nanowires for non-hierarchical external (NE) nanostructures, (2) a sea urchin nanostructure for hierarchical external (HE) nanostructures, (3) vertical cylindrical holes for non-hierarchical internal (NI) nanostructures, and (4) the imprint of sea urchin nanostructures that contain macropores as distributor channels to micro/mesostructures for hierarchical internal (HI) nanostructures. The study revealed that only the HE nanostructures provided an outstanding accessibility of active sites, although two hierarchical nanostructures possess a similar large surface area. The experimental study comparing external and internal nanostructures in the catalytic performance of DRM was reported by Zhang et al. [10]. They synthesized mesoporous silica spheres and ordered mesoporous silica (MCM-41), corresponding to NE nanostructures and NI nanostructures, respectively. They concluded that external nanostructures of mesoporous silica spheres are favorable for improving the dispersibility of the active metals and contacting between reactant molecules and active sites. However, the experimental study of HE nanostructures to provide a comprehensive understanding of the pore structure's influence on the catalytic performance remains lacking.

Dendritic mesoporous silica (DMS) is a unique class of porous materials that has the morphological characteristics of HE nanostructures and offers several advantages as catalyst supports due to its distinct characteristics [14–16]. Key features of DMS as the catalyst supports are the high surface area originating from mesopores, the tunable pore size and distribution, and the dendritic structure characterized by hierarchical branching networks [14–16]. The unique combination of these physical features makes DMS an attractive candidate for catalytic applications where efficient mass transfer and the sintering issue are essential [17]. Here, we investigated whether the macropores in DMS have an impact on DRM performance by aiding in mass transfer. For this purpose, we minimized the influence of factors affecting the DRM reaction, such as active metal size, dispersion, basicity, reducibility, and strong metal–support interaction (SMSI), and compared supports with different pore structures. The three distinct porous silica supports were prepared applying (1) a hydrothermal-assisted sol–gel method for DMS that has a macro–mesopore structure featuring a wide open-mouth morphology, (2) a spray pyrolysis-assisted sol–gel method for spray evaporation-induced self-assembly (EISA) silica with yolk–shell structured mesopores [18], and (3) an oven-assisted sol–gel method for oven EISA silica's well-developed mesopores. Subsequently, each support was impregnated with the same amount of nickel to minimize variations in factors other than the support pore structure. To evaluate the differences in pore structures among the supports, DRM activity was compared by increasing the flow rate, and physicochemical analyzes were performed to ascertain the influence of other factors.

## 2. Results and Discussion

SEM images reveal the morphologies of three distinct  $\text{SiO}_2$  supports (Figure 1). The typical morphology of layered dendritic mesoporous silica (DMS) is observed in Figure 1a,b. The DMS support was uniformly prepared with spherical particles averaging a submicron size, exhibiting a well-developed hierarchical macro–mesoporous nanostructure on the surface, as further confirmed by BET analysis. Spray EISA silica exhibits surface wrinkles, with a particle size of approximately 741 nm, larger than that of DMS (Figure 1c,d). Conversely, oven EISA silica lacks surface wrinkles, featuring macrometer-sized particles (Figure 1e,f). It exhibits a unique morphology characterized by interconnected dendritic-like structures with mesoporous channels. These structures resemble tree branches or fractal-like patterns.

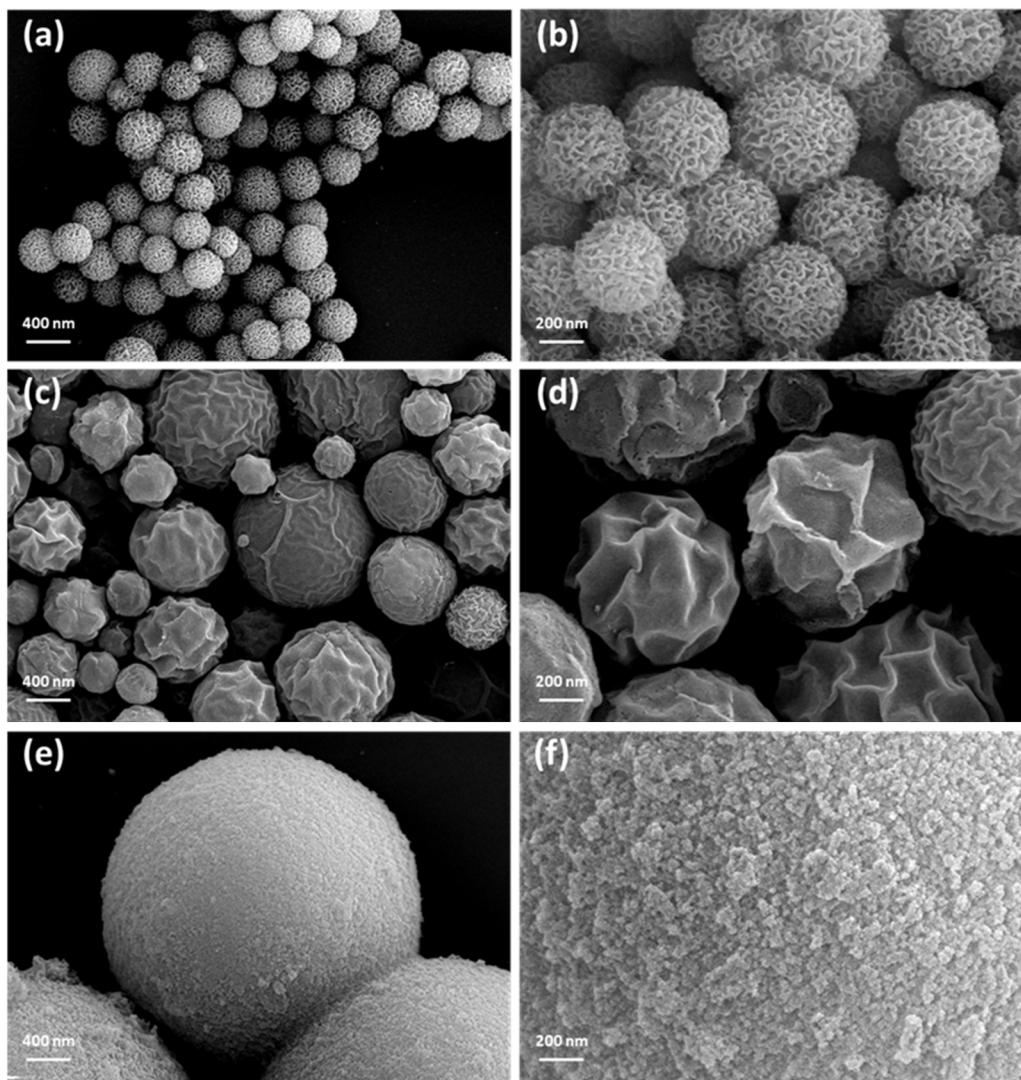


**Figure 1.** SEM images of Ni-supported DMS (a,b), spray EISA (c,d), and oven EISA silica (e,f) supports.

Metal dispersion and particle size represent two crucial factors that enhance the activity and stability of catalysts, as they can mitigate the agglomeration of active metal sites through sintering. To gain insights into the distribution of active species in the reduced catalysts, transmission electron microscopy (TEM), high-angle annular dark-field scanning TEM (HAADF-STEM), and energy-dispersive X-ray spectroscopy (EDS) mapping were conducted (Figures 2 and S1). The HAADF-STEM images reveal scattered bright spots indicating a uniform distribution of Ni nanoparticles in all three catalysts (Figure 2b,g,i). Moreover, Ni particles were uniformly dispersed in the central area of the DMS support

(Figure 2b). The nickel dispersion throughout the supports was further confirmed by EDS mapping images for all the catalyst samples (Figure 2c,h,m).

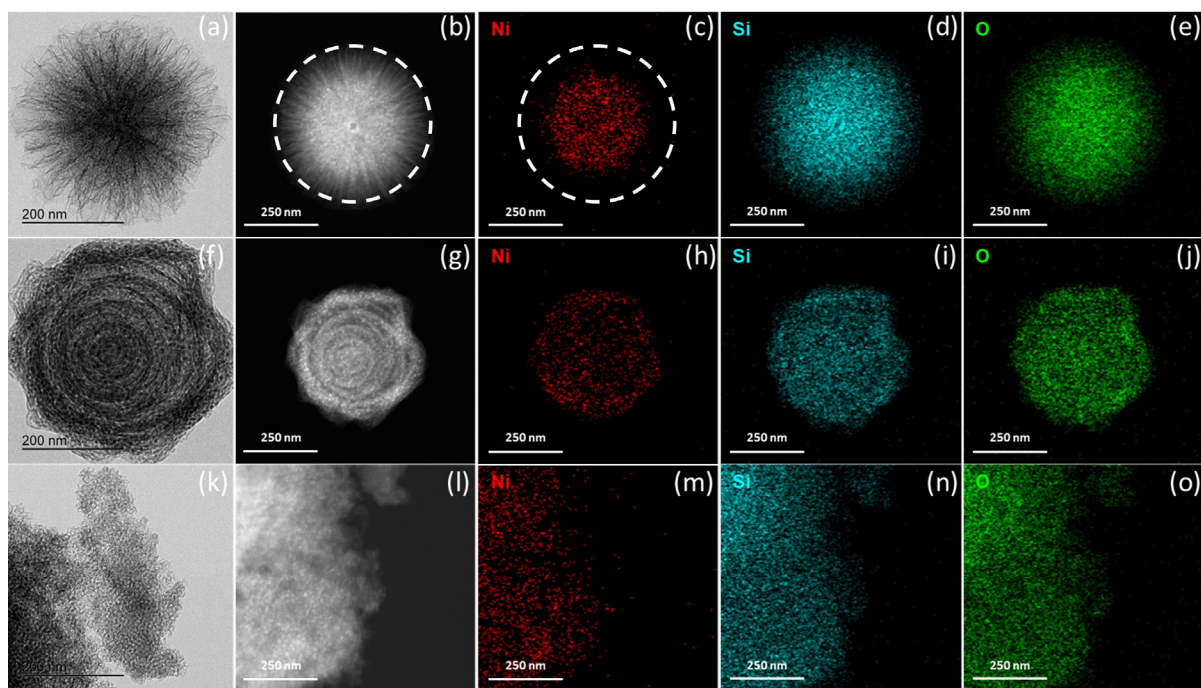


**Figure 2.** TEM (a,f,k), HAADF-STEM (b,g,l), and EDX mapping (c–e,h–j,m–o) images of reduced Ni/DMS, Ni/spray EISA, and Ni/oven EISA.

The catalytic performance of DRM is intricately linked to the physicochemical characteristics of the catalysts. These properties encompass the interaction between the active metal and the support, the dispersion and particle size of the active metal species, as well as the basicity, oxygen storage capacity, reducibility, porosity, and surface area of the catalysts [19].

It is well known that an increased specific surface area and pore volume facilitate the dispersion of active metals, thereby enhancing catalytic activity [10]. The  $N_2$  adsorption–desorption was performed by analyzing the adsorption–desorption isotherms and BJH pore size distributions of the freshly reduced Ni/SiO<sub>2</sub> catalysts (Figure 3a,b). The isotherm of the DMS support exhibits a typical, irreversible, type-IV adsorption behavior with H3 hysteresis loops at relative pressures  $P/P_0$  of 0.4 to 0.8 and 0.9 to 1.0, indicating the presence of mesopores. Correspondingly, the H3 type indicates that wedge-shaped pores have been developed. For the spray EISA silica and oven EISA silica supports, classical irreversible type-IV isotherms are observed with a hysteresis loop of the H1 type in the  $P/P_0$  range of 0.4 and 1.0, showing the formation of inkbottle-shaped pores. As presented in Figures 3b and S3, three distinct peaks in the pore size distribution curve for DMS support are observed at 3.3, 24.4, and 106.5 nm, indicating the combination of macro- and mesopores. The single narrow and strong peaks are observed for the spray EISA silica and oven EISA silica supports with pore sizes of 3.8 nm and 10.5 nm, respectively, indicating the existence of uniform mesopores. The DMS silica support has the highest pore volume among the three supports, which is attributed to the presence of macropores in the hierarchical nanostructure. Meanwhile, the oven EISA silica has the largest surface area and smallest pore diameter among the catalysts. The physical properties of the reduced Ni/DMS, Ni/spray EISA, and Ni/oven EISA catalysts are summarized in Table 1, and the characteristics of the calcined samples are presented in Table S1 and in Figure S2.

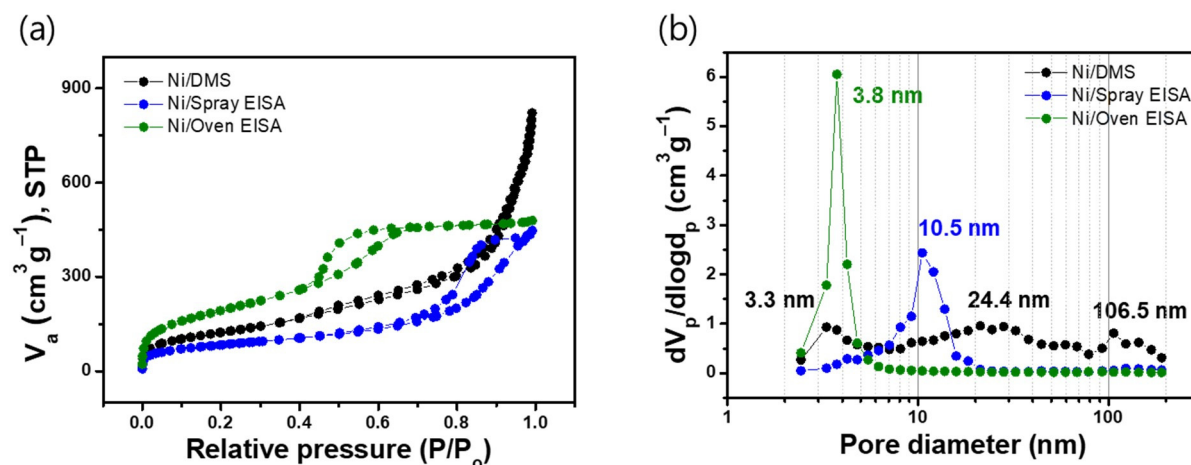


**Figure 3.** (a) N<sub>2</sub> adsorption/desorption isotherms and (b) BJH pore size distribution of the reduced Ni/DMS, Ni/spray EISA, and Ni/oven EISA.

**Table 1.** Physical properties of prepared reduced Ni/DMS, Ni/spray EISA, Ni/oven EISA catalysts.

Samples	Specific Surface Area ( $\text{m}^2/\text{g}$ )	Pore Volume ( $\text{cm}^3/\text{g}$ )	Mean Pore Size (nm)
Ni/DMS	450.0	1.24	11.0
Ni/spray EISA	304.7	0.69	9.0
Ni/oven EISA	709.0	0.74	4.2

XRD analysis was performed to investigate the Ni crystalline phase and the structure of the reduced catalyst (Figure 4). All the catalysts exhibit a typical amorphous silica peak at 22.3°, along with the characteristic diffraction peaks of metallic Ni ( $2\theta = 44.5^\circ, 51.7^\circ, 76.5^\circ$ ; PD No. 04-0850). The diffraction peaks of Ni crystallites on DMS, spray EISA, and oven EISA are weak and the widths at half the height of these peaks are large, indicating that the Ni species on all the catalysts are well dispersed. The Ni crystallite sizes of the reduced catalysts were calculated and summarized in Table 2 as Ni/DMS = 9.4 nm, Ni/spray EISA = 10.3 nm, and Ni/oven EISA = 11.6 nm, respectively, arranging in the order of Ni/DMS < Ni/spray EISA < Ni/oven EISA. The X-ray diffractograms of the calcined three catalyst samples are presented in Figure S3, showing the peaks of face-centered cubic phase NiO (JCPDS card no. #47-1049). Meanwhile, H<sub>2</sub> adsorption–desorption analysis was employed to quantify the active metallic Ni surface area and the dispersion of the freshly reduced catalysts. The Ni surface area measured by H<sub>2</sub>-pulse chemisorption follows the order of DMS < oven EISA < spray EISA. The summary of XRD and H<sub>2</sub>-pulse chemisorption data is presented in Table 2.

**Table 2.** Metallic Ni crystalline size estimated by Scherrer equation, active surface area, and metal dispersion of the freshly reduced Ni/DMS, Ni/spray EISA, and Ni/oven EISA measured by H<sub>2</sub>-pulse chemisorption.

Catalysts	XRD		H <sub>2</sub> -Pulse Chemisorption	
	Ni Crystalline Size (nm)	Metallic Ni Surface Area ( $\text{m}^2/\text{g}_{\text{cat}}$ )	Ni Dispersion (%)	Average Ni Particle Diameter (nm)
Ni/DMS	9.4	74.3	11.1	9.0
Ni/spray EISA	10.3	52.6	7.9	12.8
Ni/oven EISA	11.6	65.9	9.9	10.2

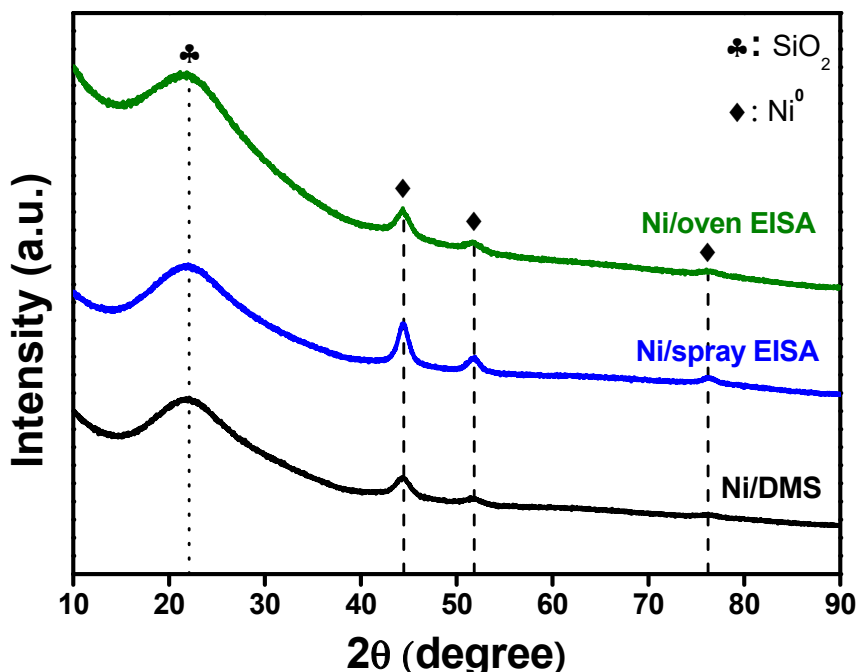


**Figure 4.** XRD patterns of reduced Ni/DMS, Ni/spray EISA, and Ni/oven EISA.

Another crucial factor contributing to the high stability of catalysts is the strong metal–support interaction (SMSI). This strong interaction plays a pivotal role in preventing Ni sintering during the DRM reaction, maintaining long-term catalytic activity with high stability. To assess the reducibility of metal-oxide-based supported catalysts and the degree of interaction between the active phase and support, the reduction behavior of three catalysts was investigated using H<sub>2</sub>-TPR analysis (Figure 5), and the H<sub>2</sub> consumption of these catalysts was quantified (Table 3). The main H<sub>2</sub>-TPR peaks observed for Ni/DMS, Ni/spray EISA, and Ni/oven EISA catalysts appeared as dual peaks at 430 °C/605 °C, 397 °C/595 °C, and 414 °C/586 °C, respectively. These two distinct reduction peaks could be ascribed to the reduction in NiO species localized in different environments [20]. The peaks at lower temperatures (430 °C, 397 °C, and 414 °C) are attributed to the reduction in bulk-phase NiO grafted onto the external surface, exhibiting higher reducibility. Meanwhile, the peaks at higher temperatures (605 °C, 595 °C, and 586 °C) are attributed to the small NiO particles embedded within the mesopores, demonstrating lower reducibility [21]. In comparison to the Ni/spray EISA and Ni/oven EISA, the reduction peaks of the Ni/DMS sample were observed at higher temperatures, suggesting lower reducibility of NiO species over Ni/DMS compared to the Ni/spray EISA and Ni/oven EISA. However, the larger peak area observed at higher temperatures for Ni/DMS in comparison to the other two catalysts indicates a stronger metal–support interaction. This suggests that hierarchical opened pore structure of DMS silica has a superior ability to confine Ni particles compared to the closed pore structure supports such as spray EISA silica and oven EISA silica.

**Table 3.** H<sub>2</sub>-TPR properties of calcined Ni/DMS, Ni/spray EISA, and Ni/oven EISA.

Samples	H <sub>2</sub> Consumption (mmol/g <sub>cat</sub> )	First Peak Area (%)	Second Peak Area (%)
Ni/DMS	0.09	34%	63%
Ni/spray EISA	0.09	46%	54%
Ni/oven EISA	0.07	52%	48%

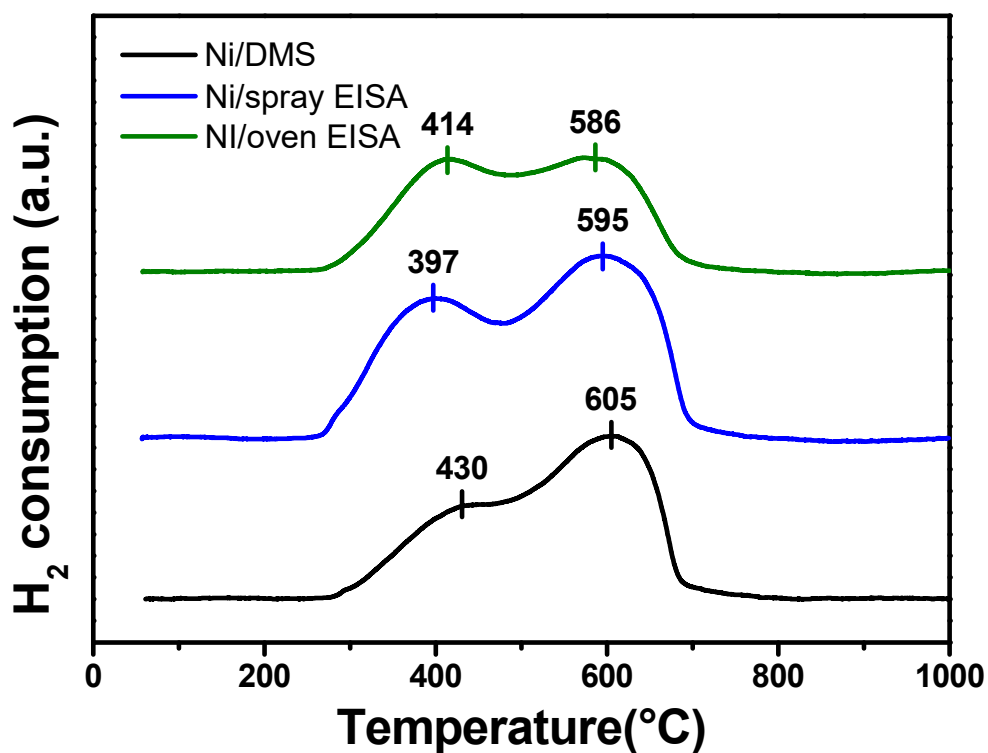


**Figure 5.**  $\text{H}_2$ -TPR profiles of calcined Ni/DMS, Ni/spray EISA, and Ni/oven EISA.

The carbon formation via  $\text{CH}_4$  decomposition is well established to occur at acid sites on the catalyst support. Therefore, basicity emerges as a pivotal property influencing the resistance of carbon formation [19]. The  $\text{CO}_2$ -TPD profile, depicted in Figure 6, illustrates desorption peaks characterized as weak ( $\text{OH}^-$ , 50–200 °C), intermediate (acid–base Lewis pair, 200–400 °C), and strong ( $\text{O}^{2-}$ , 400–800 °C) for bicarbonate, bidentate, and monodentate carbonate species, respectively [22,23]. Each catalyst exhibited a desorption peak at 200 °C, indicating weakly basic sites, such as bicarbonate species formed from the interaction between  $\text{CO}_2$  and basic surface hydroxyl groups. Meanwhile, desorption peaks observed in the 800–1000 °C temperature range correspond to strongly basic sites, including bidentate carbonate species, which interact with surface carbon species generated during methane decomposition ( $\text{CH}_4 \rightarrow \text{C} + 2\text{H}_2$ ) [24]. Notably, all three catalysts displayed comparable peaks in both the weak and strong regions, suggesting uniform basicity among them and, thus, comparable carbon formation tendencies.

The three different silica-support-based catalysts were evaluated in the DRM reaction carried out at 800 °C under the reaction gas flow rates of 90, 180, and 360  $\text{L}\cdot\text{g}^{-1}\cdot\text{h}^{-1}$ , which changed every 2 h. As is shown in Figure 7, the reaction conversion rate is inversely proportional to the gas flow rate for all the catalyst samples during the process. The average  $\text{CH}_4$  and  $\text{CO}_2$  conversion rates for each catalyst at different flow rates are presented below. At a flow rate of 90  $\text{L}\cdot\text{g}^{-1}\cdot\text{h}^{-1}$ , Ni/DMS exhibited conversion rates of 90.9% for  $\text{CH}_4$  and 96.7% for  $\text{CO}_2$ , Ni/spray EISA displayed rates of 88.8% for  $\text{CH}_4$  and 95.7% for  $\text{CO}_2$ , and Ni/oven EISA demonstrated rates of 89.9% for  $\text{CH}_4$  and 95.3% for  $\text{CO}_2$ . At 180  $\text{L}\cdot\text{g}^{-1}\cdot\text{h}^{-1}$ , Ni/DMS showed rates of 88.1% for  $\text{CH}_4$  and 93.2% for  $\text{CO}_2$ , Ni/spray EISA exhibited rates of 85.2% for  $\text{CH}_4$  and 90.2% for  $\text{CO}_2$ , and Ni/oven EISA displayed rates of 82.6% for  $\text{CH}_4$  and 87.6% for  $\text{CO}_2$ . Finally, at 360  $\text{L}\cdot\text{g}^{-1}\cdot\text{h}^{-1}$ , Ni/DMS had rates of 76.6% for  $\text{CH}_4$  and 82.1% for  $\text{CO}_2$ , Ni/spray EISA showed rates of 67.1% for  $\text{CH}_4$  and 72.8% for  $\text{CO}_2$ , and Ni/oven EISA demonstrated rates of 63.5% for  $\text{CH}_4$  and 68.6% for  $\text{CO}_2$ . All samples achieved an approximately similar  $\text{CH}_4$  conversion of 90% at a flow rate of 90  $\text{L}\cdot\text{g}^{-1}\cdot\text{h}^{-1}$ . However, as the flow rate increases from 180  $\text{L}\cdot\text{g}^{-1}\cdot\text{h}^{-1}$  to 360  $\text{L}\cdot\text{g}^{-1}\cdot\text{h}^{-1}$ , the difference in reaction conversion rate becomes significant. With increasing flow rates, the conversion of both reactants diminishes owing to the shortened contact time between the reactants

and the catalyst [25]. Across all flow rates, Ni/DMS exhibits superior conversion rates compared to Ni/spray EISA silica and Ni/oven EISA silica. This disparity is attributed to the relatively higher Ni dispersion and strong metal–support interaction (SMSI) observed in Ni/DMS. However, the conversion rate for Ni/DMS experiences a reduction of 10%, whereas for the other two mesoporous silica samples, it diminishes by as much as 20%. It can be inferred that the distinctive dendritic hierarchical nanostructure of DMS contributes to enhancing the mass transfer of the reactants and product. For the investigated samples the role of accessibility of the reactants to the catalyst active sites based on the difference in the porous structure of the supports has a significant effect on the catalytic performance in the DRM reaction.

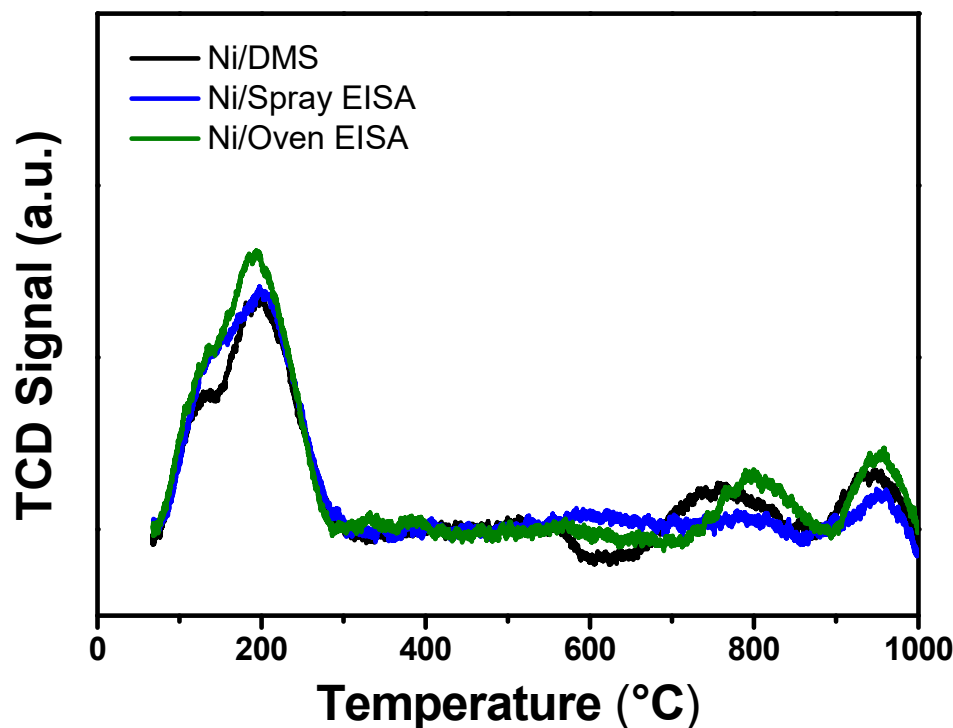


**Figure 6.**  $\text{CO}_2$ -TPD profiles of reduced Ni/DMS, Ni/spray EISA, and Ni/oven EISA.

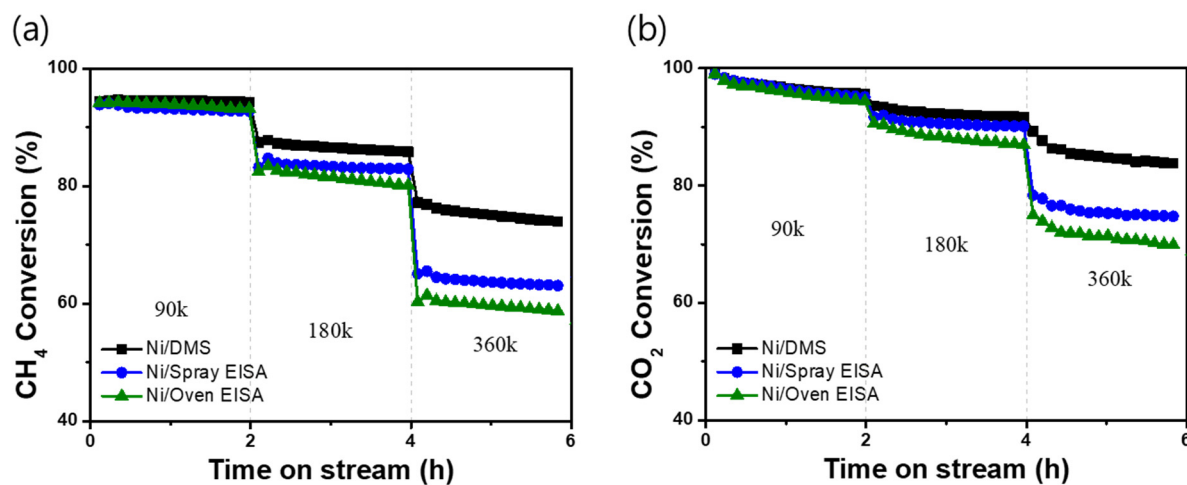


**Figure 7.** Catalytic performance of Ni/DMS, Ni/spray EISA, and Ni/oven EISA for DRM at  $800\text{ }^\circ\text{C}$ , tested for 2 h each with gas hourly space velocities (GHSV) of 90, 180, and  $360\text{ L g}_{\text{cat}}^{-1}\text{ h}^{-1}$ : (a)  $\text{CH}_4$  conversion; (b)  $\text{CO}_2$  conversion.

To evaluate the stability of the catalysts, a prolonged test was conducted at a high gas hourly space velocity of  $360 \text{ L g}_{\text{cat}}^{-1} \text{ h}^{-1}$  at  $700 \text{ }^{\circ}\text{C}$  for all three catalysts (Figure 8). Following this duration, the Ni/DMS catalyst exhibited higher conversion rates of 29.9% for  $\text{CH}_4$  and 36.9% for  $\text{CO}_2$  compared to the other catalysts. All three catalysts maintained stable conversion rates without significant deactivation throughout the 24 h period. This can be attributed to the prevention of sintering by suppressing the movement of Ni crystallites to agglomeration due to the confinement effect of the mesoporous structure common to all catalysts. The comparison of DRM performance for Ni/SiO<sub>2</sub> catalysts based on the process duration conducted at a different gas hourly space velocities is summarized in Table S2.

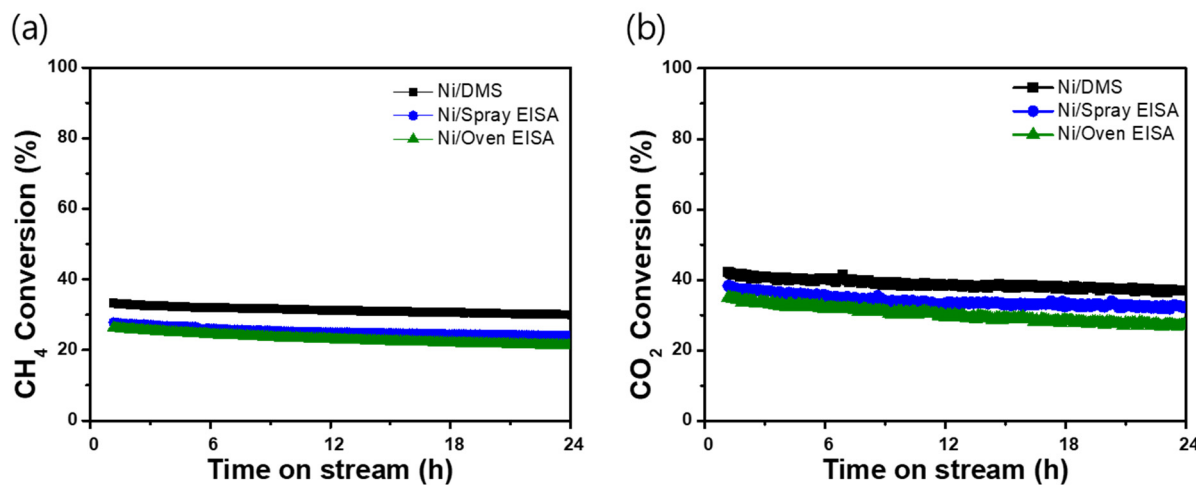


**Figure 8.** Catalytic performance of Ni/DMS, Ni/spray EISA, and Ni/oven EISA for DRM at  $700 \text{ }^{\circ}\text{C}$  for 24 h with gas hourly space velocity ( $\text{GHSV} = 360 \text{ L g}_{\text{cat}}^{-1} \text{ h}^{-1}$ ): (a)  $\text{CH}_4$  conversion; (b)  $\text{CO}_2$  conversion.

Following a 24 h stabilization test at  $700 \text{ }^{\circ}\text{C}$ , thermogravimetric analysis (TGA) was conducted to quantify the amount of coke deposition on the spent catalyst. The results are depicted in Figure 9. Weight loss within the temperature range of  $30\text{--}100 \text{ }^{\circ}\text{C}$  is presumed to be attributed to the evaporation of adsorbed water. Notably, the observed transient stage of weight gain around  $300 \text{ }^{\circ}\text{C}$  indicates nickel oxidation [26]. A slight weight loss was observed at temperatures exceeding  $330 \text{ }^{\circ}\text{C}$ , possibly indicating the combustion of accumulated carbon deposits [27] in the catalyst samples. Overall, no conspicuous weight loss peak was observed in the TGA profiles at high temperatures, suggesting the absence of carbon deposits on the catalysts.

Consequently, the Ni/DMS, Ni/spray EISA, and Ni/oven EISA catalysts exhibited stable activity without experiencing catalyst deactivation in long-term reaction tests at  $700 \text{ }^{\circ}\text{C}$ , due to their small nickel particle size and high nickel dispersion. Ni/DMS demonstrated superior conversion rates compared to the other catalysts, owing to its strong metal–support interaction and enhanced metal dispersion. In particular, it was confirmed that Ni/DMS maintained high activity even under high space velocities due to its hierarchical external macro–mesoporous nanostructure.

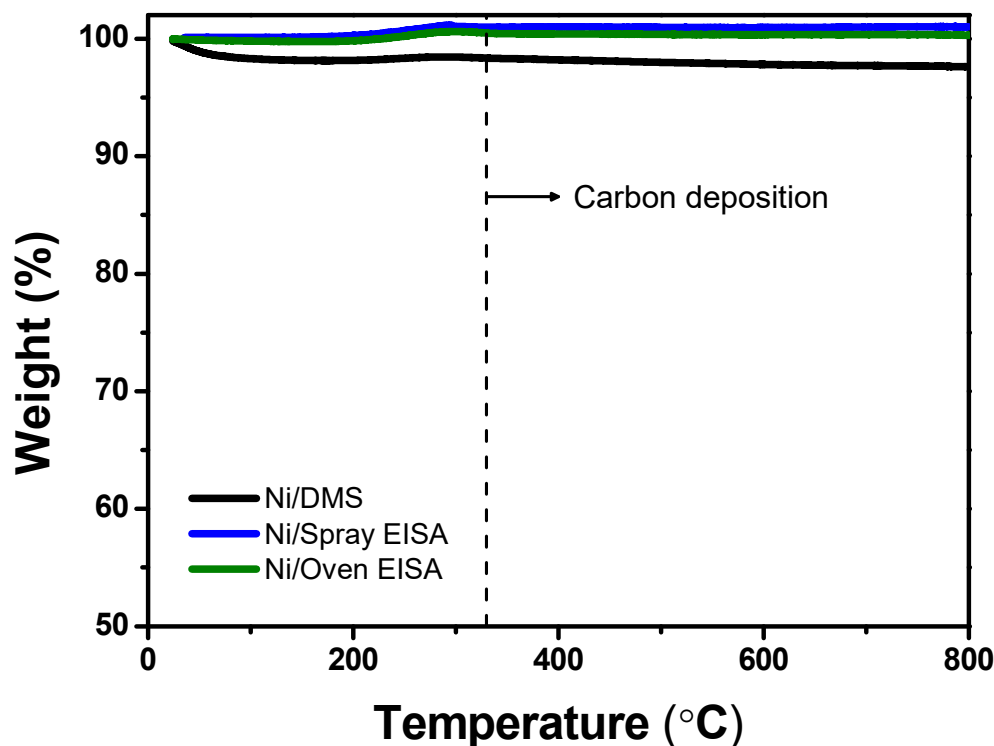


**Figure 9.** TG curves of spent Ni/DMS, Ni/spray EISA, and Ni/oven EISA catalysts.

### 3. Experimental Methodology

#### 3.1. Catalyst Preparation

##### 3.1.1. Synthesis of Dendritic Mesoporous Silica (DMS)

DMS was synthesized using a method reported elsewhere with minor modifications [17]. Firstly, 5 g hexadecyltrimethylammonium bromide (CTAB, Sigma-Aldrich, Burlington, MA, USA) and 3 g urea (99.0%, Samchun Pure Chemical Co., Ltd., Seoul, Republic of Korea) were dissolved in 150 mL of deionized water. Secondly, 150 mL cyclohexane (99.5%, Samchun Pure Chemical Co., Ltd., Republic of Korea) and 7.5 mL n-pentanol (99.0%, Samchun Pure Chemical Co., Ltd., Republic of Korea) were quickly added and stirred to form a microemulsion solution. Then, 12.5 g tetraethyl orthosilicate (TEOS, Tokyo Chemical Industry Co., Ltd., Tokyo, Japan) was added to the mixture and stirred at room temperature for 3 h. Lastly, the mixture was transferred in a Teflon-sealed autoclave (ILHAE SYSTEM, Daejeon, Republic of Korea) with a magnetic stirrer at 120 °C for 4 h with stirring at 500 rpm. After cooling, it was dried in an oven at 150 °C. The products were collected and calcined at 550 °C for 6 h to remove the organic template.

##### 3.1.2. Synthesis of Spray EISA and Oven EISA Silica Supports

First, 20 g of P123 ( $\text{EO}_{20}\text{PO}_{70}\text{EO}_{20}$ , molecular weight = 5800 g/mol, Sigma-Aldrich, USA) was added to a solution consisting of 500 mL of anhydrous ethanol (Sigma-Aldrich, USA) and 460 mL of deionized water. Then, 3.125 g of TEOS and 40 g of the 60.0% nitric acid ( $\text{HNO}_3$ , 60.0%, Samchun Pure Chemical Co., Ltd., Republic of Korea) were dissolved in the same solution. Afterward, spray EISA silica samples were obtained by the spray pyrolysis method, and oven EISA silica samples were obtained by the oven-drying method. Both products were collected and calcined at 550 °C for 6 h to remove the organic template.

##### 3.1.3. Synthesis of Ni/Silica Supported Catalysts

The as-prepared silica supports were processed through the Ni precursor impregnation using ethylene glycol as a solvent, according to the literature reported elsewhere with slight modification [21,28]. Briefly, 0.19 g nickel nitrate hexahydrate ( $\text{Ni}(\text{NO}_3)_2 \cdot 6 \text{ H}_2\text{O} \geq 98\%$ , Samchun Pure Chemical Co., Ltd. Republic of Korea) and 0.5 g DMS, spray EISA, or

oven EISA were dissolved in 10 mL ethylene glycol ( $C_2H_4(OH)_2 \geq 99.5$ , Tokyo Chemical Industry Co., Ltd. Japan), stirred overnight at room temperature, and dried in a vacuum at 80 °C until the solvent was completely evaporated. Lastly, the obtained product was calcined at 550 °C for 6 h in an air atmosphere. The resulting catalysts were indicated as Ni/DMS, Ni/spray EISA, and Ni/oven EISA. All three samples were reduced at 800 °C for 2 h under a 5%  $H_2$ /Ar atmosphere before reaction testing to obtain metallic nickel active catalytic sites.

### 3.2. Characterization

Scanning electron microscopy (SEM), using a Carl Zeiss scanning electron microscope (Merlin Compact, Zscheplin, Germany), was utilized to characterize the morphology of the catalysts. Transmission electron microscopy (TEM) images were obtained with a Tecnai G2 F30 (FEI Company, Hillsboro, OR, USA) apparatus at 300 kV. High-angle annular dark-field scanning transmission electron microscopy (HAADF-STEM) and EDX mapping analysis were performed with a AZtecTEM device (Oxford, Abingdon, UK). The surface area of each sample was calculated using the Brunauer–Emmett–Teller (BET) method with a BELSORP-mini (MicrotracBEL, Osaka, Japan). The samples were pretreated in a vacuum at 300 °C for 2 h and were then subjected to  $N_2$  adsorption–desorption at –196 °C. The pore size distribution was analyzed according to the Barrett–Joymer–Halenda (BJH) theory. X-ray diffraction (XRD) analysis was performed using an AXS D8 diffractometer (Bruker, Billerica, MA, USA) at a  $Cu K\alpha$  wavelength, 40 kV, and 40 mA. For the  $H_2$ -pulse chemisorption experiment, 50 mg of the calcined sample underwent pretreatment in a 5%  $H_2$ /Ar atmosphere at 800 °C for 2 h and was subsequently cooled to 50 °C. Following this,  $H_2$  gas was introduced to carry out the chemisorption experiment, with the assumption that the adsorption stoichiometry of  $H/Ni$  is equal to one. The reduction properties of the catalysts were analyzed by hydrogen-temperature-programmed reduction ( $H_2$ -TPR) using the BEL-CAT (MicrotracBEL, Japan). The analysis was performed at a temperature range of 50 to 1000 °C under a 5%  $H_2$ /Ar atmosphere after pretreatment at 200 °C under a He atmosphere.

### 3.3. Catalytic Reaction

Catalytic reactions were performed in a fixed-bed reactor using a quartz tube of 4 mm internal diameter, where 30 mg of quartz wool was put inside the tube before adding the catalyst layer (catalyst weight = 20 mg). The catalysts were initially subjected to pelletization under 200 Bar pressure, followed by grinding and sieving through a mesh size of 125–180 µm. Before the reaction, the calcined powder was reduced to 800 °C for 2 h at a ramping rate of 5 °C/min and a flow rate of 100 sccm ( $H_2/N_2 = 1/24$ ) to obtain the active phase ( $Ni^0$ ). The feed gases were then changed to  $CH_4$ ,  $CO_2$ , and  $N_2$  at a molar ratio of 1:1:1 and  $P = 1.0$  atm, where the flow rate was increased every 2 h to 10, 20, and 40 mL/min for each gas. The reaction was performed at  $T = 800$  °C for 6 h. The total gas hourly space velocity (GHSV) was 90, 180, and 360  $L g_{cat}^{-1} h^{-1}$ . The reaction temperature was controlled with a thermocouple located axially at the center of the catalyst bed. The effluent was quantified by online gas chromatography (HP 6890 GC, Agilent Technologies Inc., Santa Clara, CA, USA) equipped with a Carboxen-1000 packed column (Supelco 12390-U, Sigma-Aldrich, Burlington, MA, USA) and a thermal conductivity detector. The  $CH_4$  and  $CO_2$  conversions were calculated using the following equations:

$$CH_4 \text{ conversion}(\%) = \frac{[CH_4]_{in} - [CH_4]_{out}}{[CH_4]_{in}} \times 100,$$

$$CO_2 \text{ conversion}(\%) = \frac{[CO_2]_{in} - [CO_2]_{out}}{[CO_2]_{in}} \times 100,$$

where  $[CH_4]_{in}$  and  $[CH_4]_{out}$  are the inlet and outlet volume flows of  $CH_4$  gas, respectively.

#### 4. Conclusions

The examination of the performance of Ni/DMS, Ni/spray EISA, and Ni/oven EISA catalysts in the dry reforming of methane (DRM) reaction indicates superior efficiency of the hierarchical external nanostructured silica-support-based Ni/DMS sample. Ni/DMS exhibits a dual-level pore structure, combining macro- and mesoporosity. Ni/DMS exhibited remarkable activity owing to the uniform dispersion, high density, and small size of the active Ni metal particles. The revealed strong metal–support interaction confirmed by H<sub>2</sub>-TPR is an additional crucial factor in enhanced DRM reaction performance. Moreover, the macropore structure of DMS facilitates the mass transfer of reactants and the reaction products, exhibiting high CH<sub>4</sub> and CO<sub>2</sub> conversion rates even under high space velocity (GHSV) values. The featured macro–mesoporous geometry suppresses Ni particles sintering, thus enhancing the catalytic stability throughout the long-term reaction test. This study reveals that the macro–mesoporosity of the DMS support catalysts significantly influences the physicochemical properties of the Ni/DMS catalyst and plays a crucial role in the performance of the DRM reaction.

**Supplementary Materials:** The following supporting information can be downloaded at: <https://www.mdpi.com/article/10.3390/catal14040265/s1>; Figure S1: TEM image of reduced Ni/DMS; Figure S2: (a) N<sub>2</sub> adsorption/desorption isotherms and (b) pore size distribution of the calcined Ni/DMS, Ni/Spray EISA, and Ni/Oven EISA; Figure S3: XRD patterns of calcined Ni/DMS, Ni/Spray EISA, and Ni/Oven EISA; Table S1: Physical properties of prepared calcined Ni/DMS, Ni/Spray-EISA and Ni/Oven-EISA catalysts. Table S2: Comparison of DRM performance for Ni/SiO<sub>2</sub> catalysts based on the process duration.

**Author Contributions:** Conceptualization, Y.J.K. and M.-J.K.; Data curation, Y.J.K.; Formal analysis, Y.J.K.; Funding acquisition, K.L.; Investigation, Y.J.K.; Methodology, Y.J.K. and K.L.; Project administration, K.L.; Resources, K.L.; Supervision, A.M. and K.L.; Validation, A.M. and K.L.; Visualization, Y.J.K.; Writing—original draft, Y.J.K.; Writing—review and editing, Y.J.K., D.H.K., A.M. and K.L. All authors have read and agreed to the published version of the manuscript.

**Funding:** This study was supported by the New and Renewable Energy Core Technology Program of the Korea Institute of Energy Technology Evaluation and Planning (KETEP) granted financial resource from the Ministry of Trade, Industry and Energy, Republic of Korea (No. 20213030040500). This study was also supported by the Korea Institute of Energy Technology Evaluation and Planning (KETEP) grant, funded by the Korean government (MOTIE) (20214000000090, Fostering Human Resources Training in Advanced Hydrogen Energy Industry).

**Data Availability Statement:** Data are contained within the article and Supplementary Materials.

**Conflicts of Interest:** The authors declare no conflicts of interest.

#### References

1. Biswas, S.; Kulkarni, A.P.; Giddey, S.; Bhattacharya, S. A Review on Synthesis of Methane as a Pathway for Renewable Energy Storage with a Focus on Solid Oxide Electrolytic Cell-Based Processes. *Front. Energy Res.* **2020**, *8*, 570112. [[CrossRef](#)]
2. Al-Otaibi, F.; Xiao, H.; Berrouk, A.S.; Polychronopoulou, K. Numerical Study of Dry Reforming of Methane in Packed and Fluidized Beds: Effects of Key Operating Parameters. *ChemEngineering* **2023**, *7*, 57. [[CrossRef](#)]
3. Chein, R.; Yang, Z. Experimental Study on Dry Reforming of Biogas for Syngas Production over Ni-Based Catalysts. *ACS Omega* **2019**, *4*, 20911–20922. [[CrossRef](#)] [[PubMed](#)]
4. Ingale, P.; Guan, C.; Krahnert, R.; Naumann d’Alnoncourt, R.; Thomas, A.; Rosowski, F. Design of an Active and Stable Catalyst for Dry Reforming of Methane via Molecular Layer Deposition. *Catal. Today* **2021**, *362*, 47–54. [[CrossRef](#)]
5. Torimoto, M.; Sekine, Y. Effects of Alloying for Steam or Dry Reforming of Methane: A Review of Recent Studies. *Catal. Sci. Technol.* **2022**, *12*, 3387–3411. [[CrossRef](#)]
6. Le Saché, E.; Reina, T.R. Analysis of Dry Reforming as Direct Route for Gas Phase CO<sub>2</sub> Conversion. The Past, the Present and Future of Catalytic DRM Technologies. *Prog. Energy Combust. Sci.* **2022**, *89*, 100970. [[CrossRef](#)]
7. Han, K.; Yu, W.; Xu, L.; Deng, Z.; Yu, H.; Wang, F. Reducing Carbon Deposition and Enhancing Reaction Stability by Ceria for Methane Dry Reforming over Ni@SiO<sub>2</sub>@CeO<sub>2</sub> Catalyst. *Fuel* **2021**, *291*, 120182. [[CrossRef](#)]
8. Song, Q.; Ran, R.; Wu, X.; Si, Z.; Weng, D. Dry Reforming of Methane over Ni Catalysts Supported on Micro- and Mesoporous Silica. *J. CO<sub>2</sub> Util.* **2023**, *68*, 102387. [[CrossRef](#)]

9. Klaewkla, R.; Arend, M.; Hoelderich, W.F. A Review of Mass Transfer Controlling the Reaction Rate in Heterogeneous Catalytic Systems. In *Mass Transfer—Advanced Aspects*; Nakajima, H., Ed.; InTech: London, UK, 2011; ISBN 978-953-307-636-2.
10. Zhang, Y.; Zhang, G.; Liu, J.; Li, T.; Wang, Y.; Zhao, Y.; Li, G.; Zhang, Y. Dry Reforming of Methane over Ni/SiO<sub>2</sub> Catalysts: Role of Support Structure Properties. *Fuel* **2023**, *340*, 127490. [[CrossRef](#)]
11. Li, H.; Wang, J.; Chen, C.; Jia, L.; Hou, B.; Li, D. Effects of Macropores on Reducing Internal Diffusion Limitations in Fischer-Tropsch Synthesis Using a Hierarchical Cobalt Catalyst. *RSC Adv.* **2017**, *7*, 9436–9445. [[CrossRef](#)]
12. Wang, G.; Coppens, M.-O. Rational Design of Hierarchically Structured Porous Catalysts for Autothermal Reforming of Methane. *Chem. Eng. Sci.* **2010**, *65*, 2344–2351. [[CrossRef](#)]
13. Al-Halhouli, M.; Kieninger, J.; Yurchenko, O.; Urban, G. Mass Transport and Catalytic Activity in Hierarchical/Non-Hierarchical and Internal/External Nanostructures: A Novel Comparison Using 3D Simulation. *Appl. Catal. Gen.* **2016**, *517*, 12–20. [[CrossRef](#)]
14. Shen, D.; Chen, L.; Yang, J.; Zhang, R.; Wei, Y.; Li, X.; Li, W.; Sun, Z.; Zhu, H.; Abdullah, A.M.; et al. Ultradispersed Palladium Nanoparticles in Three-Dimensional Dendritic Mesoporous Silica Nanospheres: Toward Active and Stable Heterogeneous Catalysts. *ACS Appl. Mater. Interfaces* **2015**, *7*, 17450–17459. [[CrossRef](#)] [[PubMed](#)]
15. Xue, X.-L.; Lang, W.-Z.; Yan, X.; Guo, Y.-J. Dispersed Vanadium in Three-Dimensional Dendritic Mesoporous Silica Nanospheres: Active and Stable Catalysts for the Oxidative Dehydrogenation of Propane in the Presence of CO<sub>2</sub>. *ACS Appl. Mater. Interfaces* **2017**, *9*, 15408–15423. [[CrossRef](#)] [[PubMed](#)]
16. Gu, Q.; Jiang, P.; Shen, Y.; Zhang, K.; Wai, P.T.; Haryono, A. High-Dispersed MoO<sub>3</sub> Nanoparticles in 3D-Dendritic Mesoporous Silica Nanospheres: Heterogeneous Catalysts for the Epoxidation of Olefins. *J. Porous Mater.* **2021**, *28*, 779–789. [[CrossRef](#)]
17. Peng, H.; Zhang, X.; Han, X.; You, X.; Lin, S.; Chen, H.; Liu, W.; Wang, X.; Zhang, N.; Wang, Z.; et al. Catalysts in Coronas: A Surface Spatial Confinement Strategy for High-Performance Catalysts in Methane Dry Reforming. *ACS Catal.* **2019**, *9*, 9072–9080. [[CrossRef](#)]
18. Choi, S.H.; Kang, Y.C. Synergetic Effect of Yolk–Shell Structure and Uniform Mixing of SnS–MoS<sub>2</sub> Nanocrystals for Improved Na-Ion Storage Capabilities. *ACS Appl. Mater. Interfaces* **2015**, *7*, 24694–24702. [[CrossRef](#)] [[PubMed](#)]
19. Jang, W.-J.; Shim, J.-O.; Kim, H.-M.; Yoo, S.-Y.; Roh, H.-S. A Review on Dry Reforming of Methane in Aspect of Catalytic Properties. *Catal. Today* **2019**, *324*, 15–26. [[CrossRef](#)]
20. Molina, R.; Poncelet, G.  $\alpha$ -Alumina-Supported Nickel Catalysts Prepared from Nickel Acetylacetone: A TPR Study. *J. Catal.* **1998**, *173*, 257–267. [[CrossRef](#)]
21. Xie, T.; Shi, L.; Zhang, J.; Zhang, D. Immobilizing Ni Nanoparticles to Mesoporous Silica with Size and Location Control via a Polyol-Assisted Route for Coking- and Sintering-Resistant Dry Reforming of Methane. *Chem. Commun.* **2014**, *50*, 7250–7253. [[CrossRef](#)]
22. Xu, Y.; Wu, Y.; Li, J.; Wei, S.; Gao, X.; Wang, P. Combustion-Impregnation Preparation of Ni/SiO<sub>2</sub> Catalyst with Improved Low-Temperature Activity for CO<sub>2</sub> Methanation. *Int. J. Hydrg. Energy* **2021**, *46*, 20919–20929. [[CrossRef](#)]
23. Singha, R.K.; Yadav, A.; Agrawal, A.; Shukla, A.; Adak, S.; Sasaki, T.; Bal, R. Synthesis of Highly Coke Resistant Ni Nanoparticles Supported MgO/ZnO Catalyst for Reforming of Methane with Carbon Dioxide. *Appl. Catal. B Environ.* **2016**, *191*, 165–178. [[CrossRef](#)]
24. Huang, X.; Ni, C.; Zhao, G.; Irvine, J.T.S. Oxygen Storage Capacity and Thermal Stability of the CuMnO<sub>2</sub>–CeO<sub>2</sub> Composite System. *J. Mater. Chem. A* **2015**, *3*, 12958–12964. [[CrossRef](#)]
25. Aranda-Aguirre, A.; Ojeda, J.; Ferreira De Brito, J.; Garcia-Segura, S.; Boldrin Zanoni, M.V.; Alarcon, H. Photoelectrodes of Cu<sub>2</sub>O with Interfacial Structure of Topological Insulator Bi<sub>2</sub>Se<sub>3</sub> Contributes to Selective Photoelectrocatalytic Reduction of CO<sub>2</sub> towards Methanol. *J. CO<sub>2</sub> Util.* **2020**, *39*, 101154. [[CrossRef](#)]
26. Ji, K.; Meng, F.; Xun, J.; Liu, P.; Zhang, K.; Li, Z.; Gao, J. Carbon Deposition Behavior of Ni Catalyst Prepared by Combustion Method in Slurry Methanation Reaction. *Catalysts* **2019**, *9*, 570. [[CrossRef](#)]
27. Le, T.A.; Kim, M.S.; Lee, S.H.; Park, E.D. CO and CO<sub>2</sub> Methanation over Supported Cobalt Catalysts. *Top. Catal.* **2017**, *60*, 714–720. [[CrossRef](#)]
28. Zhang, X.; Zhang, L.; Peng, H.; You, X.; Peng, C.; Xu, X.; Liu, W.; Fang, X.; Wang, Z.; Zhang, N.; et al. Nickel Nanoparticles Embedded in Mesopores of AISBA-15 with a Perfect Peasecod-like Structure: A Catalyst with Superior Sintering Resistance and Hydrothermal Stability for Methane Dry Reforming. *Appl. Catal. B Environ.* **2018**, *224*, 488–499. [[CrossRef](#)]

**Disclaimer/Publisher’s Note:** The statements, opinions and data contained in all publications are solely those of the individual author(s) and contributor(s) and not of MDPI and/or the editor(s). MDPI and/or the editor(s) disclaim responsibility for any injury to people or property resulting from any ideas, methods, instructions or products referred to in the content.